Highly Active Iridium/Iridium−Tin/Tin Oxide Heterogeneous Nanoparticles as Alternative Electrocatalysts for the Ethanol Oxidation Reaction

Wenxin Du,[†] Qi Wang,[§] David Saxner,[||] N. Aaron Deskins,[||] Dong Su,[⊥] James E. Krzanowski,[‡] Anatoly I. Frenkel,[#] and Xiaowei Teng*,[†]

[†]Department of Chemical Engineering and [‡]Department of Mechanical Engineering, University of New Hampshire, Durham, New Hampshire 03824, United States

[§]Department of Chemical Engineering, University of Delaware, Newark, Delaware 19716, United States

[||]Department of Chemical Engineering, Worcester Polytechnic Institute, 100 Institute Road, Worcester Massachusetts 01609, United States

[⊥]Center for Functional Nanomaterials, Brookhaven National Laboratory, Upton, New York 11973, United States

[#]Department of Physics, Yeshiva University, New York, New York 10016, United States

S *Supporting Information*

ABSTRACT:
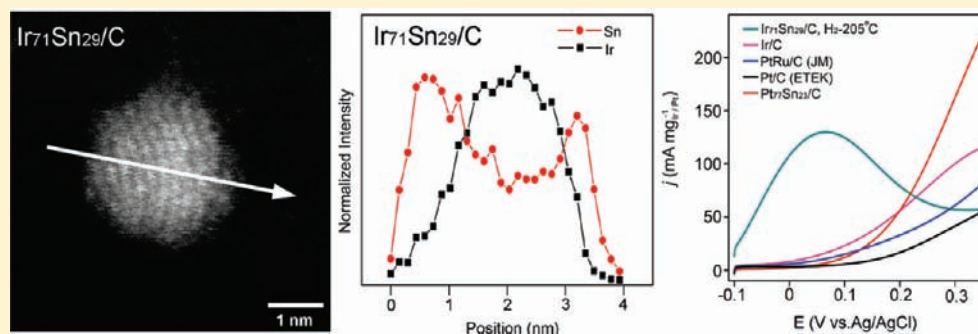
Ethanol is a promising fuel for low-temperature direct fuel cell reactions due to its low toxicity, ease of storage and transportation, high-energy density, and availability from biomass. However, the implementation of ethanol fuel cell technology has been hindered by the lack of low-cost, highly active anode catalysts. In this paper, we have studied Iridium (Ir)-based binary catalysts as low-cost alternative electrocatalysts replacing platinum (Pt)-based catalysts for the direct ethanol fuel cell (DEFC) reaction. We report the synthesis of carbon supported $Ir_{71}Sn_{29}$ catalysts with an average diameter of 2.7 ± 0.6 nm through a "surfactant-free" wet chemistry approach. The complementary characterization techniques, including aberration-corrected scanning transmission electron microscopy equipped with electron energy loss spectroscopy, X-ray diffraction, X-ray photoelectron spectroscopy, and X-ray absorption spectroscopy, are used to identify the "real" heterogeneous structure of $Ir_{71}Sn_{29}$/C particles as Ir/Ir−Sn/SnO_2, which consists of an Ir-rich core and an Ir−Sn alloy shell with SnO_2 present on the surface. The $Ir_{71}Sn_{29}$/C heterogeneous catalyst exhibited high electrochemical activity toward the ethanol oxidation reaction compared to the commercial Pt/C (ETEK), PtRu/C (Johnson Matthey) as well as PtSn/C catalysts. Electrochemical measurements and density functional theory calculations demonstrate that the superior electro-activity is directly related to the high degree of Ir−Sn alloy formation as well as the existence of nonalloyed SnO_2 on surface. Our cross-disciplinary work, from novel "surfactant-free" synthesis of Ir−Sn catalysts, theoretical simulations, and catalytic measurements to the characterizations of "real" heterogeneous nanostructures, will not only highlight the intriguing structure−property correlations in nanosized catalysts but also have a transformative impact on the commercialization of DEFC technology by replacing Pt with low-cost, highly active Ir-based catalysts.

1. INTRODUCTION

Rising demands for energy, coupled with concerns over environmental pollution and growing fossil fuels cost, pose great needs for clean and efficient power sources. Since the energy conversion efficiency of heat engines is confined by Carnot cycle limitation (typically <35%), the electrochemical oxidation of small organic molecules (SOMs) becomes attractive due to its high thermodynamic efficiency (higher than 70%) and low emission of CO_2 footprint via low-temperature direct fuel cell

reactions.[1−3] Compared to hydrogen and methanol, ethanol is a promising fuel in the so-called direct ethanol fuel cell (DEFC) reaction for several reasons:[4−9] (1) Ethanol is less toxic; (2) ethanol is easy to store and transport due to its relatively higher boiling point; (3) ethanol has higher energy density due to the nature of 12 electron transfer upon complete oxidation; and (4) ethanol has been qualified as a substantial energy source since it can be produced in large quantities from sugar- and cellulose-containing raw materials. However, the implementation of the DEFC technology has been hindered by the sluggish ethanol oxidation reaction (EOR) at the anode, due to the lack of an active anode catalyst.

Platinum (Pt) and its alloys are the most common catalysts in both anode and cathode fuel cell reactions because of their excellent properties in the adsorption and dissociation of SOMs.[1,2,4,10−19] However, the expense of Pt-based catalysts is a major impediment in the commercialization of fuel cell technology, since Pt-based catalysts alone account for approximately 54% of the total fuel cell stack cost.[20,21] Development of alternative electrocatalysts with high activity to EOR and low-cost is vital for the implementation of DEFC technology. Several Pd-based catalysts have been proposed as alternatives to Pt in the oxygen reduction reaction (cathode reaction) or in the anode reaction in alkaline fuel cells.[22−25] However, developing effective Pt-free anode catalysts for ethanol oxidation in an acidic electrolyte remains a challenge.

A frequently used strategy to design highly active catalysts in proton-exchange membrane fuel cells (PEMFCs) is the use of multicomponent catalysts, including random alloys,[2,5,26] intermetallic alloys,[13,14] near surface alloys (nonrandom alloys),[27,28] or core/shell particles.[16−18,29,30] The electro-activity of multicomponent catalysts is determined not only by the intrinsic properties of the metal components but also by their synergistic interactions, which are known as ligand (responsible for the charge transfer between the components), ensemble (responsible for the adsorption properties due to the presence of distinct atomic groups), and geometric (three-dimensional structural characteristics) effects. The synergistic effect of multicomponent metal catalysts has also been successfully explained by the changes of electronic band structure. The d-band model developed by Nørskov and co-workers has successfully correlated the strength of adsorbate bonding for the rate-limiting step to the electronic structure of the catalysts and therefore to the reaction activity.[31,32] Recently, Strasser et al. showed that de-alloyed Cu−Pt core−shell nanoparticles appeared to have compressive lattice strain, which further caused the down shift of the d-band center of the Pt atoms and therefore weakened the bonding to the reactive intermediates, resulting in enhanced activity in the oxygen reduction reaction.[18] Hence, carefully tailoring the geometry, ligand and/or ensemble effects of multicomponent heterogeneous catalysts could lead to development of an alternative catalyst replacing expensive Pt for the fuel cell reactions.

Iridium (Ir) has been used as an additive in Pt/C catalysts for hydrogen evolution and oxidation of hydrocarbon reactions.[33,34] Ir metal is less expensive ($890/oz) than Pt ($1864/oz).[35] To date, several Ir−M (M: Se, V, Co, Sn) electrocatalysts have been reported for fuel cell reactions.[36−39] These results are encouraging. However, the lack of structural and spectroscopic information for Ir-based systems hinders mechanistic interpretation and direct comparison with other well characterized Pt-based catalysts for fuel cell reactions.

In addition to the difficulty in finding active, low-cost electrocatalysts for the DEFC reaction, the synthesis of effective nanocatalysts is also challenging. Solution phase synthesis is the most commonly used method for the preparation of nanomaterials, which normally involves a surfactant that achieves fine control over the size and shape of the catalysts. However, surfactant residue on the surface of the catalysts is not easily removed even after vigorously rinsing. Therefore, a "surfactant-free" synthesis is necessary to yield "clean" catalysts in solution, while still maintaining the size and uniformity of the catalysts. Herein, we report the "surfactant-free" synthesis of carbon supported Ir−Sn alloys with an average diameter of less than 3 nm. Using complementary characterization techniques, we have identified the formation of an Ir−Sn alloy which strongly depends on the composition of Ir and Sn. The electrochemical activity of Ir−Sn/C toward the EOR has been studied, and our results unambiguously indicate the promotional effect of alloy formation on the EOR activity.

2. EXPERIMENTAL SECTION

2.1. Synthesis of Ir−Sn/C Nanoparticles. In a typical synthesis of $Ir_{71}Sn_{29}$ nanoparticles, 33.3 mg $SnCl_2$ (Alfa Aesar, 99%) was initially dissolved in 11 mL of ethylene glycol (EG, AR, Mallinckrodt Chemicals) with 1 mL of deionized water. The mixture was then heated up to 130 °C for 1 h. $IrCl_3 \cdot xH_2O$ (0.1 mmol, 35.3 mg, Alfa Aesar, 99.9%) was first dissolved in the 3 mL of EG solution and then injected into 8 mL of preheated EG (130 °C) in a flask which contained appropriate aliquots of tin (0.025 mmol) colloidal solution. The reaction proceeded for 2 h under an argon flow. The as made $Ir_{71}Sn_{29}$ particles were then mixed with 125 mg of carbon black (Vulcan XC−72, specific surface area of 254 m^2/g) via magnetic stirring for 1 h at room temperature. The formation of Ir−Sn nanoparticles without surfactant capping might be attributed to a coordination effect of glycolic acid resulting from the oxidation of ethylene glycol, as reported previously in the synthesis of PtRu nanoparticles.[40] The as made Ir−Sn/C was then treated in a hydrogen/argon flow at 205 °C for 1 h to evaporate any possible ethylene glycol residual and to reduce any possible ionic Sn and promote Ir/Sn alloy formation.

2.2. Structural Characterizations. High-resolution transmission electron microscopy (HRTEM) was carried out with a FEI Titan 80−300 at 300 kV. High-angle angular dark-field (HAADF) STEM images and electron energy loss spectroscopy (EELS) measurements were performed and collected using aberration-corrected Hitachi HD 2700C equipped with a modified Gatan Enfina ER spectrometer at the Center for Functional Nanomaterials at the Brookhaven National Laboratory. Regular TEM images were taken using a Zeiss/LEO 922 Omega TEM. X-ray diffraction (XRD) patterns were recorded by a Bruker AXS instrument equipped with a general area detector diffraction system (GADDS) detector. A Cu Kα X-ray tube was employed as X-ray source. X-ray photoelectron spectroscopy (XPS) was conducted using a Kratos Axis HS XPS system with a Mg anode as the X-ray source.

2.3. XAS Measurements. XAS experiments were conducted at beamline X18B at the National Synchrotron Light Source, Brookhaven National Laboratory. The operating storage ring energy was 2.5 GeV, and the ring current was between 110 and 300 mA. A pellet was mounted in the in situ cell, which was placed between two ionization chambers for data collection in transmission mode. The in situ experiments were carried out at the Sn K edge (29 200 eV) and Ir L_3 edges (11 215 eV). The sample was first heated to 205 °C and kept for one hour under the 5% H_2/He flow, then heated to 300 °C and kept for two hours. Afterward, the sample was cooled to room temperature, all under a 5%H_2/He flow. In the air, the sample was heated to 50 °C and held for 1 h. After cooling down to room temperature in the air, the sample was

then heated in air to 250 °C and kept for 1 h. The in situ process was monitored by X-ray absorption near edge structure (XANES) measurements at both Sn K and Ir L_3 edges, while the extended X-ray absorption fine structure (EXAFS) scans were taken in the steady state at each reaction stage. The Ir black and Sn foil standards were measured simultaneously along with the measurements of the samples, respectively, by placing the standards between the transmitted beam detector and the reference detector, for X—ray energy calibration and data alignment. The IFEFFIT package was used to carry out data processing and analysis.[41]

2.4. Electrochemical Measurements. The electrochemical properties were examined with a CHI 660 single channel electrochemical workstation (CH Instruments). A three-electrode system, which was composed of a glassy carbon rotating disk electrode (RDE) as the working electrode, a platinum wire counter electrode, and an Ag/AgCl (1 M KCl) reference electrode, was employed for the test. The rotating rate of the working electrode was controlled at 1000 rpm. Supported catalysts were dispersed in deionized water, and 10 μL of catalyst ink (containing 2—4 μg of Ir or Pt) was drop casted on the working electrode. Upon drying, another 10 μL of Nafion solution (0.5%, V_{Nafion}/V_{water}) was used to cover the catalysts. The Nafion will cover the electrocatalysts on the surface of electrode. It will prevent the catalyst from detachment without affecting the transport of the reactants and products during the electrooxidation of ethanol. Cyclic voltammetry (CV) was performed in argon-purged 0.5 M sulfuric acid (99.999%, Sigma-Aldrich) with the electrolyte scanning from −0.25 to 0.35 V at a scan rate of 30 mV/s to collect hydrogen (H) adsorption/desorption information on the catalyst surface. The electrocatalytic activity of these catalysts toward ethanol oxidation was evaluated through CV and current density vs time measurements in 0.5 M of ethanol/0.5 M of sulfuric acid electrolyte at room temperature. The quasi-steady-state polarization curve from linear sweep voltammetry (LSV) performed at a sweep rate of 1 mV s^{-1} in 0.5 M of ethanol/0.5 M of H_2SO_4 solution was used for the Tafel plot. The electrolyte was deaerated by bubbling argon for 30 min prior to the measurements.

2.5. DFT Calculations. All density functional theory (DFT) calculations were performed with the CP2K code,[42,43] which uses the Gaussian and plane waves (GPW) method.[44] Goedecker—Tetter—Hutter-type pseudopotentials represented core electrons.[45,46] Valence electrons were treated by optimized basis sets that describe the condensed phase well.[47] All metals were represented by double-ζ basis sets, while C, O, and H were represented by triple-ζ basis sets. The Perdew, Burke, and Ernzerhof (PBE) exchange—correlation functional was used in all calculations.[48] CP2K uses periodic boundary conditions and samples reciprocal space at the Γ point. All calculations were spin polarized.

To explore the issue of Sn alloying with Ir, we modeled nanoparticles of Ir with some atoms replaced by Sn. The nanoparticles were place in a large box with dimensions of 27 × 27 × 27 Å. Decomposition of ethanol was simulated over model surfaces of Ir, Sn, and Ir/Sn. The surfaces used for ethanol decomposition were treated by clusters (see Figure 8). Because CP2K samples only the Γ point, large slabs are needed to ensure a proper k-point density and to obtain reasonable results within the slab approach.[49] Cluster models however allow for a smaller surface structure to be modeled and are therefore computational more tractable. Furthermore, cluster models can give results that are in good agreement with slab calculations, such as those using a plane-wave basis set.[50,51] Our own tests (see the Supporting Information) show that agreement with plane-wave simulations is indeed possible with clusters of an appropriate size. A (110) SnO_2 surface was modeled using a periodic slab model with a (4 × 2) surface cell. Further details of the DFT calculations are found in the Supporting Information.

3. RESULTS AND DISCUSSION

3.1. Synthesis and Structural Characterizations of $Ir_{71}Sn_{29}$/C Catalysts.
Figure 1a shows the TEM image of $Ir_{71}Sn_{29}$

electrocatalysts after being reduced at 205 °C, which are uniformly distributed throughout the carbon support with an average size of 2.7 + 0.6 nm (Figure S1, Supporting Information, energy dispersive X-ray spectroscopy). Figure 1b shows well-defined lattice fringes of $Ir_{71}Sn_{29}$/C, which can be attributed to {111} planes of a cubic Ir alloy structure. Figure 1c and d shows the EELS line scans of Ir and Sn from a typical ~3 nm supported $Ir_{71}Sn_{29}$ nanoparticle, acquired from an aberration-corrected STEM. Normalized intensity profiles show a higher signal intensity of Sn at the edges compared to the center of the particle, in contrast to the Ir profile that appears as a "volcano" shape. The EELS line scan profiles of Ir and Sn suggests a Sn shell-rich and Ir core-rich heterogeneous structure. The EELS measurements from different $Ir_{71}Sn_{29}$ particles also confirm the nonrandom distribution of Ir and Sn within the individual particle (Figure S2, Supporting Information). Further evidence comes from XPS measurements (Figure S3, Supporting Information): the perfect match of binding energies for Sn $3d_{5/2}$ (486.7 eV) and $3d_{3/2}$ (495.1 eV) between $Ir_{71}Sn_{29}$ and commercial SnO_2 unambiguously shows the presence of ionic Sn (SnO_2) on the surface.

Carbon-supported $Ir_{71}Sn_{29}$ shows a broad but clear diffraction pattern from the XRD analysis (Figure 2). Two distinguishable peaks at 40.4° and 67.7° are attributed to (111) and (220) planes of a face-centered cubic (FCC) structure. The peak around 25° belongs to (002) planes of carbon black. Compared to the Ir/C catalysts made via a similar approach, the (111) diffraction peak of $Ir_{71}Sn_{29}$ shifts to a lower 2θ angle by 1.3°, in good agreement with the alloying of Sn into Ir. Similar expansion of the lattice structures is also observed in the PtSn alloy.[52−55] Although EELS and XPS indicate the presence of ionic Sn (SnO_2) on the surface, XRD did not show the existence of the SnO_2 on the surface. Anomalies of SnO_2 in the diffraction data can be explained by the overwhelming signal from Ir heavy metal or the incomplete lattice formation (amorphous structure) as was reported in Pd-doped Sn/SnO_x nanoparticles previously.[56]

3.2. XANES and EXAFS Analyses.
XANES measurements were used to investigate the electronic states of the Ir and Sn in the as-made $Ir_{71}Sn_{29}$ catalyst in different gas atmospheres at the elevated temperatures. Figure 3a shows that the Sn K-edge absorption peak region of the as-made $Ir_{71}Sn_{29}$/C is similar to that of SnO_2, suggesting that Sn is strongly oxidized. After reduction (205 °C for 1 h), the Sn K-edge data of $Ir_{71}Sn_{29}$ in the XANES region (near edge) are similar to those of Sn foil, indicating a metallic state for Sn. Meanwhile, the Sn K-edge data in the EXAFS region (extended edge) are different from those of Sn foil, hinting at the formation of IrSn alloy, in agreement with the results derived from the XRD measurements. After the reduced $Ir_{71}Sn_{29}$ was exposed to air at room temperature, Sn K-edge XANES spectra showed features of cationic Sn, suggesting the formation of Sn oxide. The electronic structure was monitored by in situ XANES during these processes and depicted in Figure S4, Supporting Information.

On the other hand, the Ir L_3 edge absorption data of the as-made $Ir_{71}Sn_{29}$/C features a white line with the intensity between that of Ir foil and IrO_2, whereas the XAFS oscillations resemble to that of metallic foil with relatively lower amplitude, indicating predominantly metallic phase of Ir metal with Ir oxide on the surface (Figure 3b). After reduction, the Ir L_3 white line is considerably lower than that in the as-made sample, indicating the removal of surface layer of the Ir oxide. Since white-line features in the Ir L_3 edge arise from 2p to 5d dipole transitions,

15174

dx.doi.org/10.1021/ja205649z |*J. Am. Chem. Soc.* 2011, 133, 15172–15183
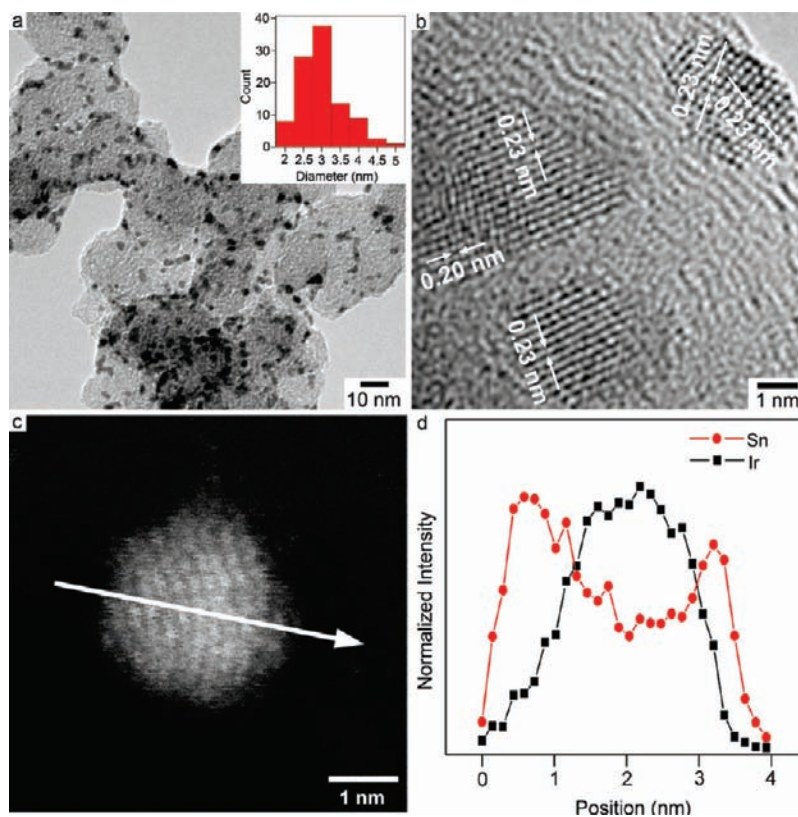
Figure 1. (a) TEM, (b) HRTEM, and (c) HAADF images of the carbon-supported $Ir_{71}Sn_{29}$ catalyst after reduction in H_2/Ar flow. (d) EELS line scans across individual the $Ir_{71}Sn_{29}$ nanoparticle, as indicated by white arrows in (c). The inset in (a) shows particle size distribution.
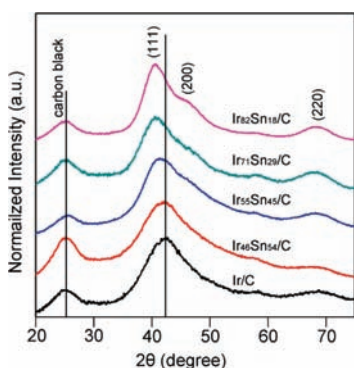
Figure 2. XRD patterns of carbon-supported Ir, $Ir_{46}Sn_{54}$, $Ir_{55}Sn_{45}$, $Ir_{71}Sn_{29}$, and $Ir_{82}Sn_{18}$ nanoparticles after reduction at 205 °C under H_2/Ar flow.

low white-line intensity in the reduced $Ir_{71}Sn_{29}/C$ points to a more filled d-band. The modified d-band feature may result from the alloying of Sn, as suggested previously for a PtSn alloy.[57−59] More interestingly, only a slight increase was observed in the Ir white-line intensity, even after the followed drastic oxidation procedure (250 °C for 2 h), correlating very well with the proposal that Ir mainly exists in the core of the structure.

In order to analyze the exact compositions of the Sn and SnO_2 inside the $Ir_{71}Sn_{29}/C$ catalyst, XANES linear combination fitting (LCF) analysis was performed using the Athena program. Figure 3c and d shows the XANES spectra under reduced and oxidized conditions together with the best fit from the linear

combination of the data measured in the Sn foil and SnO_2 nanoparticles (40 nm in diameter). When the Ir−Sn was reduced at 205 °C for 1 h, the metallic Sn content was found to be ~84% of the available Sn, indicating where the predominant Sn metal was located in the $Ir_{71}Sn_{29}/C$ catalyst. Therefore, the overall composition of $Ir_{71}Sn_{29}$ can be expressed as "$Ir_{71}Sn_{29\times84\%} - Sn_{29\times(1-84\%)}O_X = Ir_{71}Sn_{24} - Sn_5O_X$". When the sample was exposed to the air flow at 250 °C for 1 h, the Sn metal content was found to be only ~11%, or indicating the catalyst to have the composition as "$Ir_{71}Sn_{29\times11\%} - Sn_{29\times(1-11\%)}O_X = Ir_{71}Sn_3 - Sn_{26}O_X$". These results indicate that Sn oxide formation is much enhanced in an oxidizing environment but still present in a reducing environment.

To explore the structural details, EXAFS analysis was conducted for both reduced and oxidized $Ir_{71}Sn_{29}$ catalysts using the Artemis program. Fitting was performed simultaneously for Ir and Sn edges' data while applying several physically reasonable constraints (Table 1). In addition, several k-weighting factors were used in the fit, whenever appropriate, to minimize the correlation between fitting parameters (Figure S5, Supporting Information). Results of the FEFF6 fits, conducted simultaneously for the Sn K- and Ir-L_3 edges' data for (a) as-made sample, (b) reduced sample at 205 °C, and (c) oxidized sample at 250 °C are depicted in Figure S5, Supporting Information. The best-fit values of structural parameters for all conditions are listed in Table 1.

Table 1 and Figure S5, Supporting Information indicate that Ir exists mainly in the metallic phase with Ir−O bonds decorating the surface in the as-made $Ir_{71}Sn_{29}/C$, while Sn predominantly

15175

dx.doi.org/10.1021/ja205649z |*J. Am. Chem. Soc.* 2011, 133, 15172–15183
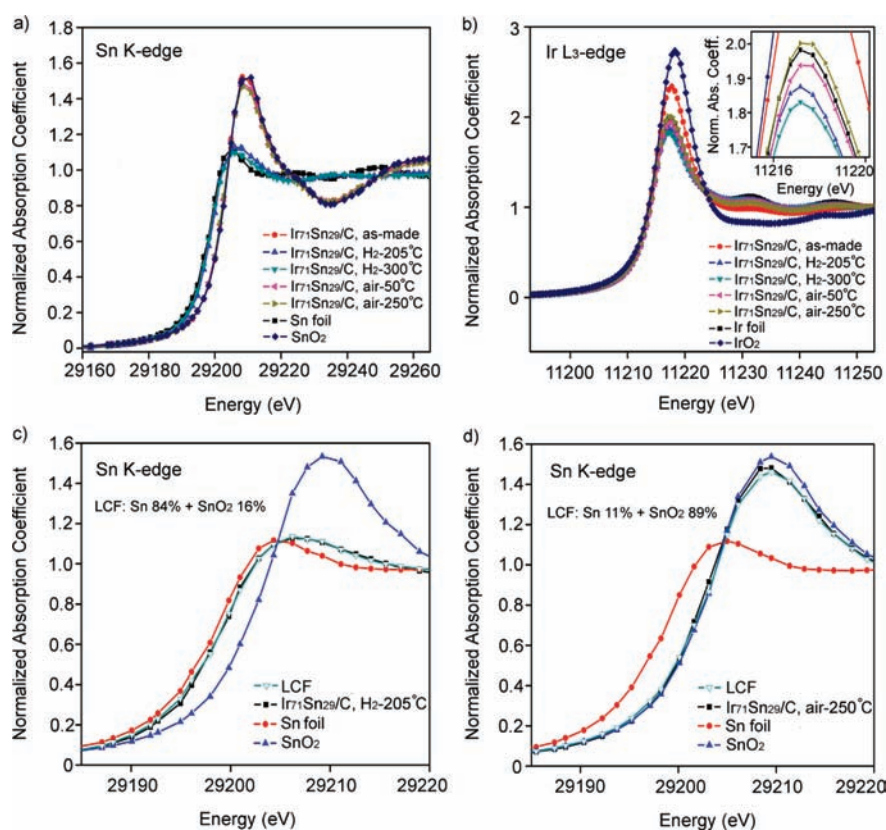
Figure 3. Selected XANES spectra of (a) Sn K-edge and (b) Ir L_3-edge of $Ir_{71}Sn_{29}$/C during the reduction in H_2/He flow and oxidation in air flow at different temperatures; (c) LCF of $Ir_{71}Sn_{29}$/C after reduction at 205 °C under H_2/He flow and (d) LCF fit of $Ir_{71}Sn_{29}$/C after oxidation at 250 °C under air flow.

Table 1. Ir−Sn System EXAFS Data Fitting Result (with X_{Sn}/X_{Ir} Constraints)

	Ir	Sn	$Ir_{71}Sn_{29}$/C, as-made	$Ir_{71}Sn_{29}$/C H_2, 205 °C	$Ir_{71}Sn_{29}$/C H_2, 300 °C	$Ir_{71}Sn_{29}$/C, air 50 °C	$Ir_{71}Sn_{29}$/C, air 250 °C	SnO_2
N_{Ir-Ir}	12		6.2 (5)	9.2 (4)	8.8 (5)	9.2 (7)	8.7 (8)	
N_{Ir-O}			3.5 (5)			1.2 (1.8)	0.8 (4)	
N_{Ir-Sn}					1.5 (5)^a	0.9 (1.8)^a		
N_{Sn-Sn}		4	1.5 (1.4)	0.5 (4)	0.9 (4)	1.5 (6)	1.5 (9)	2
N_{Sn-O}			7.4 (5)	1.5 (5)	0.2 (2)	6.7 (2)	6.3 (4)	6
N_{Sn-Ir}				4.2 (7)	3.7 (5)	2.4 (1.8)		
R_{Ir-Ir} (Å)	2.715 (1)		2.684 (3)	2.693 (2)	2.696 (3)	2.696 (4)	2.688 (4)	
R_{Ir-O} (Å)			1.998 (7)			1.98 (5)	1.98 (2)	
R_{Ir-Sn} (Å)					2.74 (1)^b	2.85 (5)^b		
R_{Sn-Sn} (Å)		3.020 (2)	3.24 (2)	3.06 (3)	3.09 (3)	3.249 (9)	3.24 (2)	3.204 (3)
R_{Sn-O} (Å)			2.062 (6)	2.08 (2)	2.13 (4)	2.061 (4)	2.055 (6)	2.063 (2)
R_{Sn-Ir} (Å)				2.75 (2)	2.74 (1)	2.85 (5)		
σ^2_{Ir-Ir} (Å^2)	0.0035 (1)		0.0064 (2)	0.0058 (2)	0.0066 (3)	0.0053 (3)	0.0065 (4)	
σ^2_{Ir-O} (Å^2)			0.008 (1)			0.02 (3)	0.003 (4)	
σ^2_{Ir-Sn} (Å^2)					0.013 (2)^b	0.02 (1)^b		
σ^2_{Sn-Sn} (Å^2)		0.0105 (4)	0.0076 (5)	0.001 (5)	0.010 (7)	0.006 (2)	0.007 (4)	0.0022 (3)
σ^2_{Sn-O} (Å^2)			0.0056 (8)	0.016 (8)	0.00 (1)	0.0061 (5)	0.0071 (9)	0.0027 (4)
σ^2_{Sn-Ir} (Å^2)				0.012 (3)	0.013 (2)	0.02 (1)		

^{a} Indicates the following constraint was used: $N_{Ir-Sn} = N_{Sn-Ir} \times X_{Sn}/X_{Ir}$. ^{b} Indicates the following constraint was used: $R_{Ir-Sn} = R_{Sn-Ir}$; $\sigma^2_{Ir-Sn} = \sigma^2_{Sn-Ir}$.
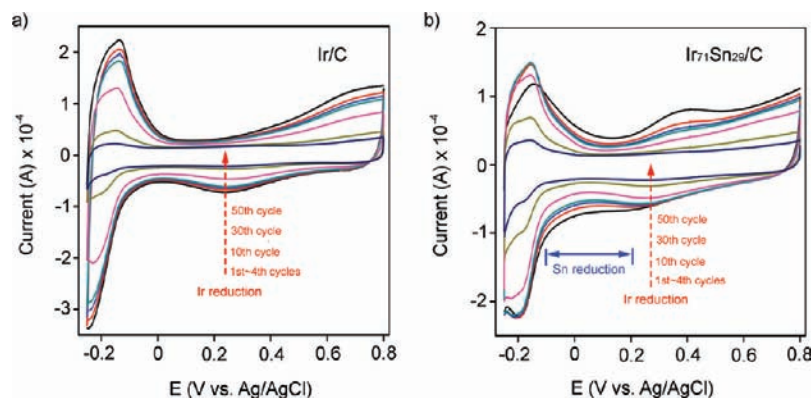
Figure 4. CVs of (a) Ir/C and (b) $Ir_{71}Sn_{29}$/C in acid-only electrolyte sweeping from -0.25 to 0.8 V.

exists in the oxide form. The former conclusion stems from the fact that the Ir–Ir bond distance (2.684 ± 0.003 Å) is more similar to that in a pure Ir crystal (2.715 ± 0.001 Å) rather than that in an IrO_2 structure (3.115 Å). The latter conclusion stems from the similarity between the average bond distances measured in our EXAFS analyses for the Ir–Sn alloy ($R_{Sn-Sn} = 3.24 \pm 0.02$ Å) and the SnO_2 ($R_{Sn-Sn} = 3.204 \pm 0.003$ Å). The resulting coordination number of Sn–O ($N_{Sn-O} = 7.4 \pm 0.5$), exceeds somewhat the coordination number (6) in SnO_2. This discrepancy may be attributed to the correlation of the coordination numbers and the bond length disorder in the fit.

Table 1 and Figure S5, Supporting Information also show that metallic structures dominate both Ir and Sn in the reduced $Ir_{71}Sn_{29}$/C (205 °C in the H_2/He flow). The higher resultant Ir–metal (Ir–M) coordination number ($N_{Ir-M} = N_{Ir-Ir} + N_{Ir-Sn} = 9.2 \pm 0.4$) relative to that of Sn–M ($N_{Sn-M} = N_{Sn-Ir} + N_{Sn-Sn} = 4.7 \pm 0.8$) points to the model that has an Ir-rich core and a Sn-rich shell, since such a configuration will cause the Sn environment to be less coordinated by metallic neighbors than the Ir environment, due to the surface truncation effects.[60] In addition to the Sn–M coordination number being smaller than that of Ir–M, significant Sn–O contribution is an independent evidence for a Sn-rich shell.

By examining partial coordination numbers for Ir–Ir, Ir–Sn, Sn–Ir, and Sn–Sn pairs, we confirmed this model and further refined it by proposing a more detailed scenario of Ir and Sn segregation. Specifically, we obtained that Ir L_3-edge EXAFS data are contributed by predominantly monometallic Ir, while the Sn environment is, on the average, heterogeneous: ($N_{Sn-Ir} = 4.2 \pm 0.7$) and ($N_{Sn-Sn} = 0.5 \pm 0.4$). This observation further refines our core–shell structure model: the core consists mostly of monatomic Ir, while the shell is composed of an Ir–Sn alloy. The coexistence of the separated SnO_2 and Ir/Ir–Sn nanoparticles can be excluded by the facts that no SnO_2 phase was observed in the XRD pattern (Figure 2) and that only an Ir core-rich, Sn shell-rich structure was observed by STEM-EELS line scans (Figure 1 and Figure S2, Supporting Information) from several individual particles without the observation of separated SnO_2 nanoparticles.

Very similar Ir–Sn heterogeneous structures arise after the $Ir_{79}Sn_{21}$/C was reduced at 300 °C in the H_2/He flow. The Ir–M coordination number ($N_{Ir-M} = N_{Ir-Ir} + N_{Ir-Sn} = 10.3 \pm 0.7$) is much higher than Sn–M coordination ($N_{Sn-M} = N_{Sn-Ir} + N_{Sn-Sn} = 4.6 \pm 0.6$). The relatively larger difference between N_{Ir-M} and N_{Sn-M} compared to that obtained in the sample being

reduced at 205 °C suggests an even more segregated Ir–Sn structure (Ir-rich core and Sn-rich shell). Such phenomenon can be explained by the lower surface free energy of Sn relative to Ir, which drives Sn to the surface at elevated temperatures.

After the reduced Ir–Sn/C was oxidized at 250 °C in the air, no distinguishable Ir–Sn (N_{Ir-Sn}) and Sn–Ir (N_{Sn-Ir}) coordination could be observed. Large Sn–O coordination was obtained ($N_{Sn-O} = 6.3 \pm 0.4$), indicating most of Sn transforms to SnO_2. On the other hand, Ir retains its metallic character, although a small amount of Ir–O bonding is present, demonstrated by XANES analysis (described above) and EXAFS analysis ($N_{Ir-O} = 0.8 \pm 0.4$).

The results from EXAFS and XANES analysis reveal the intriguing dynamics of Ir/Sn heterogeneous atoms at the nanoscale: as-made $Ir_{71}Sn_{29}$/C shows strong segregation with slightly oxidized Ir and highly oxidized Sn (SnO_2) within the nanoparticles. Once reduced at 205 and 300 °C, a high level of Ir–Sn alloy forms, resulting from the migration of Sn atoms into the Ir lattice, and after consequent oxidation at 250 °C in the air, Ir–Sn/C again appears as phase segregation between Ir and SnO_2.

3.3. Electrochemical Measurements of $Ir_{71}Sn_{29}$/C in EOR. Given the heterogeneous nature of the Ir–Sn catalyst, the electrochemical activity of the $Ir_{71}Sn_{29}$/C catalysts toward the ethanol oxidation reaction was evaluated, in order to interpret the structure–function relationship in Ir–Sn/C catalysts.

The CV of Ir/C and $Ir_{71}Sn_{29}$/C catalysts in acidic solution are shown in Figure 4 with the sweeping potentials between -0.25 and 0.8 V (vs Ag/AgCl). During the cathodic scans, reduction peaks of Ir (as red arrow marked) diminished continuously. Steady-state CV was reached after 50 cycles of potential sweeping. Similar decreases in the voltammetric charges were observed in $Ir_{71}Sn_{29}$/C catalysts during the sweeping. Since Nafion was used to cover the catalysts on the surface of electrode, the possibility of catalysts detachment can be excluded. Therefore, we believe the decreases in voltammetric charges may indicate a significant change in the roughness of the surfaces of Ir and Ir–Sn, possibly due to the irreversible aggregation on the surface of both catalysts during the high potential sweeping. After 50 cycles of CV scans at the potentials between -0.25 and 0.8 V, the electrochemical active surface area (ECSA) of $Ir_{71}Sn_{29}$/C decreased from 2.6 cm^2 to 0.66 cm^2 with respective to 3 μg Ir metal loading, showing 75% loss. On the other hand, ECSA of Ir/C decreased from 3.2 to 0.32 cm^2 under the same condition, showing 90% loss. $Ir_{71}Sn_{29}$/C catalysts also showed discernible Sn reduction features (as blue arrow marked) between -0.1 and
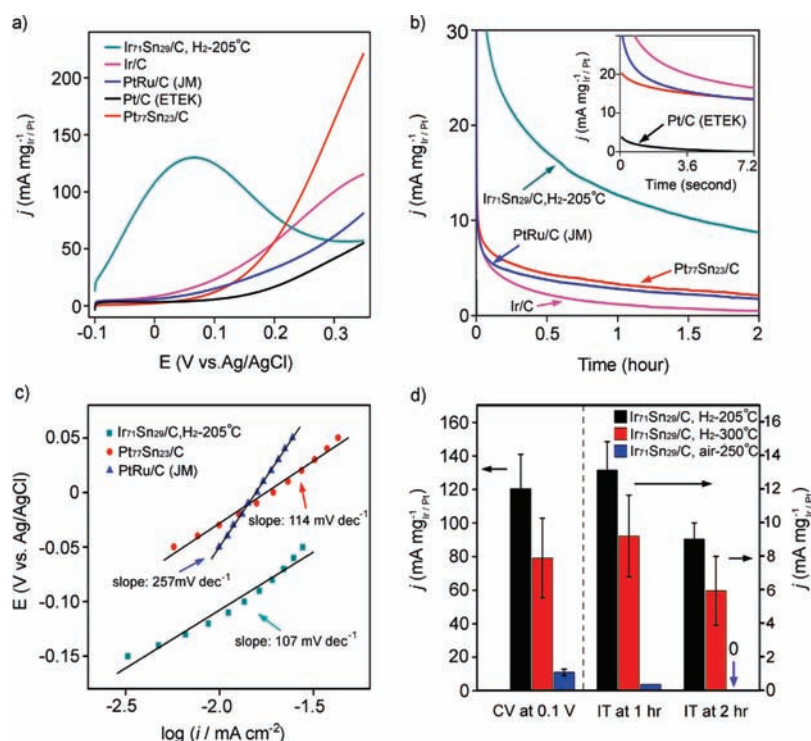
Figure 5. Electrochemical measurements of carbon-supported $Ir_{71}Sn_{29}$, Ir, and $Pt_{77}Sn_{23}$ and Pt (ETEK), PtRu (JM) catalysts: (a) CVs from $-0.1 \sim 0.35$ V and (b) current density vs time measurements at 0.1 V in 0.5 M of H_2SO_4/0.5 M of ethanol electrolyte, (c) Tafel plot for ethanol electrooxidation on $Ir_{71}Sn_{29}$/C, $Pt_{77}Sn_{23}$/C, and PtRu (JM) catalysts in 0.5 M of H_2SO_4/0.5 M of ethanol electrolyte at scan rate of 1 mV s^{-1} (data extracted from LSV measurements), and (d) comparisons of CV and current density vs time measurements between $Ir_{71}Sn_{29}$/C reduced in H_2/Ar at 205 °C, $Ir_{71}Sn_{29}$/C reduced in H_2/Ar at 300 °C, and $Ir_{71}Sn_{29}$/C oxidized in air at 250 °C conducted at the same conditions as in (a) and (b) .

0.2 V in the cathodic scans compared to Ir/C. The continuous decrease of voltammetric charges in this region could be attributed to the dissolution of the Sn component during potentials sweeping. These features show that metallic Sn exists in the $Ir_{71}Sn_{29}$/C catalysts as an Ir—Sn alloy structure, which is subject to oxidation at high potentials. Similar etching of the Sn component was also observed in a PtRhSn ternary alloy catalyst we reported recently.[61]

The instability found in both catalysts upon high potential sweeping may due to their small sizes (both catalysts are less than 3 nm). To improve its stability in the high potential, one could increase the size of Ir—Sn. Meanwhile, our data indicate that SnO_2 on the surface may stabilize the Ir—Sn/C, as seeing less ECSA loss in Ir—Sn/C compared to Ir/C under the same condition. Therefore, introducing a metal oxide support may also offer a solution to stabilize Ir—Sn/C and Ir/C small catalysts.[62]

The CV curves (forward scans) of $Ir_{71}Sn_{29}$/C in the solution of 0.5 M of H_2SO_4/0.5 M of ethanol are shown in Figure 5a in the presence of Ir/C, $Pt_{77}Sn_{23}$/C, and commercial Pt/C (20 wt %, ETEK) and PtRu/C [Johnson Matthey (JM), 30 wt % Pt, 15 wt % Ru] electrocatalysts. The positive potentials are limited to 0.35 V to avoid the dissolution of the Sn. Figure 5a shows a low peak potential during ethanol oxidation of $Ir_{71}Sn_{29}$/C (at 0.07 V), compared to those of Ir/C, $Pt_{77}Sn_{23}$/C, PtRu/C (JM), and Pt/C (ETEK). In particular, the $Ir_{71}Sn_{29}$/C sample exhibits a peak mass current density of 130 mA/mg Ir at a potential of 0.07 V, which is 11 and 30 times higher than those of commercial PtRu/C and Pt/C, respectively.

Current density vs time measurements were conducted in a solution of 0.5 M of H_2SO_4/0.5 M of ethanol with a constant applied potential at 0.1 V for 2 h. For all five current density vs

time curves displayed in Figure 5b, the current drops continually with time, which could be due to the poisoning of surface active sites. $Ir_{71}Sn_{29}$/C catalysts show a superior long-term activity with a mass current density of 8.7 mA/mg Ir after 2 h reaction, while the Ir/C, $Pt_{77}Sn_{23}$/C and PtRu/C only exhibit 0.6, 2.2, and 1.8 mA/mg Pt (or Ir), respectively. Commercial Pt/C was inactive under such a low steady potential (0.1 V). The current of Pt/C dropped to zero within seconds of reaction.

Figure 5c shows a linear region of the Tafel plots measured in the solution of 0.5 M of H_2SO_4/0.5 M of ethanol with a scan rate of 1 mV s^{-1} of the $Ir_{71}Sn_{29}$/C, $Pt_{77}Sn_{23}$/C, and PtRu/C (JM) catalysts. The lowest Tafel slope (107 mV dec^{-1}) found in $Ir_{71}Sn_{29}$/C indicates a high rate of ethanol electrooxidation. Similar anodic Tafel slopes of 114 mV dec^{-1} were obtained from $Pt_{77}Sn_{23}$/C catalysts, suggesting that the same reaction mechanism occurs for both catalysts containing Sn. Tafel slopes on both catalysts are in agreement with the Temkin-type adsorption for both OH_{ad} (*OH) and ethoxi (*CH_3CO) at low potentials, indicating reaction ($CH_3CO + OH \rightarrow CH_3COOH$) is the rate-determining step for the EOR at low potentials.[63] In contrast, ethanol oxidation on PtRu/C (JM) surface showed a much higher anodic Tafel slope (257 mV dec^{-1}), suggesting a lower charge-transfer rate during the EOR.

3.4. Optimum Sn Content in Ir—Sn/C Catalysts. We have studied in total four different carbon supported Ir—Sn bimetallic nanoparticles with the atomic ratios of Sn ranging from 18 to 54% (Figure S8, Supporting Information). The strains (S) of various Ir—Sn alloys are used to characterize the level of Ir—Sn alloying, given by the equation: $S = (a_{Ir-Sn} - a_{Ir})/a_{Ir}$, from which a_{Ir-Sn} and a_{Ir} are the lattice parameters of supported FCC Ir—Sn
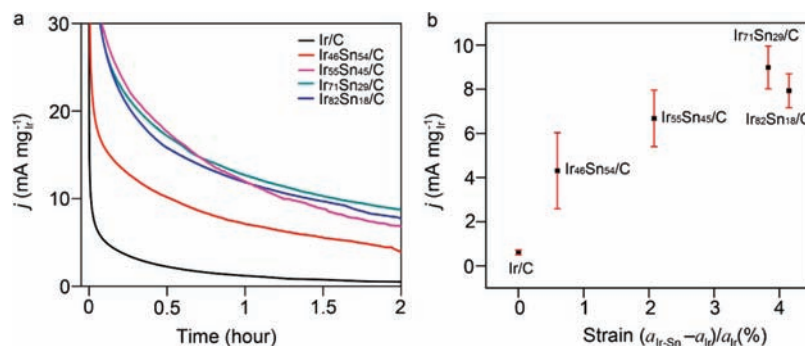
Figure 6. (a) Current density vs time measurements of Ir/C, $Ir_{46}Sn_{54}$/C, $Ir_{55}Sn_{45}$/C, $Ir_{71}Sn_{29}$/C and $Ir_{82}Sn_{18}$/C at 0.10 V in 0.5 M of H_2SO_4/0.5 M of ethanol electrolyte, and (b) plot of current density vs time activity vs strain $(a_{Ir-Sn} - a_{Ir})/a_{Ir}$ (%). Specifically, a_{Ir-Sn} is denoted as the lattice constant of each individual electrocatalyst, while a_{Ir} represents the lattice constant of home-made carbon-supported Ir nanoparticles.

and Ir nanocatalysts calculated from the (111) diffraction peaks. To examine the relationship between alloy formation and electroactivity of various Ir—Sn alloys, Figure 6 shows the current density obtained from chronoamperometric measurements as a function of the strain (S). Foremost, the data show that all the Ir—Sn catalysts had larger lattice parameters than pure Ir nanoparticles and that the strain (S) and mass current density toward EOR increased when more Sn alloyed with Ir. When the strain increased from 0.6% to 3.8%, the averaged mass current density obtained from current density vs time measurements increased from 4.3 to 9.0 mA/ mg Ir. Among the various Ir—Sn catalysts, $Ir_{71}Sn_{29}$/C and $Ir_{82}Sn_{18}$/C had higher strains (S) and catalytic activities. Meanwhile, an inverse linear relationship between Sn content and alloy strain (S) was observed. For example, $Ir_{82}Sn_{18}$/C had the largest value of strain (over 4%), while $Ir_{46}Sn_{54}$/C had the least value (0.6%), showing a "negative" deviation from Vegard's law. This could be explained by the formation of nonalloyed SnO_2 on the surface, consistent with a similar "inverse" Vegard's law found in the Pt—Rh and Pt—Ru bimetallic nanostructures reported previously where surface segregation of transition metal happened.[64,65]

Although the Ir—Sn system has been rarely studied previously, its Pt-based counterpart (Pt/Sn) has been intensively studied in the EOR from the groups of Lamy, Antolini, Behm, and Xin, with controversial results on the optimum ratio of Sn.[6,26,53−55,66−71] Xin et al. reported that the optimum composition of 33−40% (molar ratio) of Sn in nonalloyed Pt—SnO$_x$ had a better performance than a Pt—Sn alloy for EOR.[67] Conversely, Behm et al reported a less alloyed Pt—Sn/C catalyst with 25% Sn showed lower EOR activity compared to commercial Pt.[72] Antolini recently predicted the theoretically optimized Sn content for the EOR in partially alloyed Pt$_x$—Sn/C catalysts for the x in the range from 1.66 to 3, representing 25−38% Sn.[71] Our data (Figure 6) showed that a maximum of ~20% metallic Sn might be able to completely alloy with Ir, where the largest strain (S) value was observed. When more Sn atoms were added, they were not fully incorporated into the Ir lattice, resulting in the surface enrichment as oxides.

To provide insight into the surface enrichment of Sn in the Ir—Sn catalysts, we have employed DFT calculations to model the stability of Sn atoms in Ir—Sn particles. Figure 7 shows optimized structures for four different Ir/Sn particles. All of these particles contained 50 atoms and approximated particles 1 nm in diameter. The structure for an Ir particle was taken from the work of Doye and Wales,[73] wherein they used a Monte Carlo algorithm

0.01 eV/atom   0.00 eV/atom

0.01 eV/atom   0.15 eV/atom
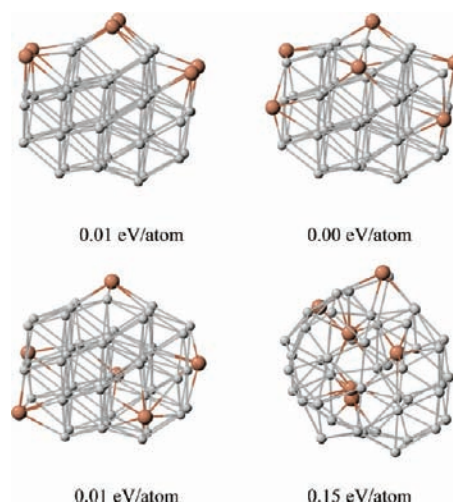
Figure 7. Calculated DFT potential structures for Ir—Sn nanoparticles. The relative energies for the particles are shown; the particle at 0 eV/atom is the most stable. The gray and brown spheres represent Ir and Sn atoms, respectively.
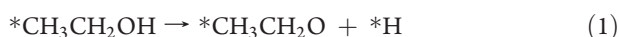
with an empirical potential to determine optimized particle structures for Pt and Rh. We took the particle geometries and reoptimized them using DFT but with Ir rather than Pt or Rh. These particular nanoparticles display large number of (111) facets, the most stable FCC surfaces, and thus provide a reasonable model representing the "real" catalyst particles. For three of the particles we took the Ir particle and substituted six Sn atoms along the surface of the particle, since the experimental results show a high concentration of Sn atoms on the surface of $Ir_{71}Sn_{29}$ nanoparticles. As we can see in Figure 7, the Sn atoms distort the surface of Ir/Sn particles extensively, and the Sn atoms move away from the surface, likely due to the poor Ir—Sn miscibility. We also modeled one particle by replacing six core Ir atoms with Sn. This particle distorted significantly, and several Sn moved to the surface during relaxation. Relative energies for the different particles were calculated (0.00 eV/atom corresponding to the most stable particle), and the Ir—Sn particle with core Sn was unstable by 0.15 eV/atom, while the Sn surface-rich particles were relatively close in energy (0.00−0.01 eV/atom). These calculations help explain why the experimentally observed carbon supported Ir—Sn particles are Sn-rich on the surface, since they show the poor mixing of Ir and Sn in the core of the particle.

3.5. Alloying Effect of Ir–Sn/C in EOR. The superior performance of binary alloy electrocatalysts has been attributed to a bifunctional effect and an electronic (ligand) effect, which have been frequently observed in many Pt-based binary catalysts. To estimate the synergistic effect of Ir–Sn alloy in EOR, the electro-activities of $Ir_{71}Sn_{29}/C$ reduced at 205 and 300 °C and oxidized at 250 °C were compared. After reduced $Ir_{71}Sn_{29}/C$ (as $Ir/IrSn/SnO_x$) was oxidized at 250 °C in the air, the mass current density of oxidized $Ir_{71}Sn_{29}/C$ only showed 10% of the value displayed by the reduced $Ir_{71}Sn_{29}/C$ (H_2, 205 °C) in CV measurements, and it eventually dropped to 0 after 2 h in IT measurement (Figure 5d). We also notice that the $Ir_{71}Sn_{29}/C$ reduced at 300 °C showed slightly decreased current density, even though it had more alloying. This can be explained by the possible aggregation of catalysts at elevated temperature.

It is also noteworthy that the current densities for ethanol oxidation shown in Figure 5d follow the same trend as the white-line intensity of the Ir L_3 adsorption edge (Figure 3b inset). For example, $Ir_{71}Sn_{29}/C$ catalysts reduced at 205 and 300 °C, which show the higher current density in EOR, had lower white-line intensity in the Ir L_3 edge relative to the Ir foil, demonstrating a more filled Ir d-band. On the other hand, $Ir_{71}Sn_{29}/C$ catalyst oxidized at 250 °C had the least activity in EOR as well as higher white-line intensity relative to Ir foil. This correlation indicates that the promoting effect of alloying between Ir–Sn is also linked to the occupancy of the Ir d-band. Increasing the amount of alloy resulted in a reduced white-line intensity, which has been interpreted in terms of smaller vacancy of the Ir 5d-band. It is known that transition metals (e.g., Sn and Ru) lead to more occupancy of the Pt d-band, which weakens the Pt–CO bond. The weakened Pt–CO bond will then enhance CO diffusion from Pt to Ru or Sn sites and allow the formation of CO_2 at lower potentials.[74−77] In this work, the electronic back donation from Sn to Ir in the Ir–Sn alloy phase changed the electronic structure of Ir, allowing the weakening of the Ir–CO bond and therefore improving catalytic performance. A higher degree of alloying found in $Ir_{71}Sn_{29}/C$ brings Ir and Sn atoms in close proximity throughout the catalysts, which could optimize both bifunctional effects and electronic modification between the two components.

3.6. DFT Calculations of Surface Reactions. In order to understand how the nature of the catalyst affects the reaction of ethanol, we modeled the first steps of ethanol decomposition and oxidation (i.e., H removal) over several potential catalyst surfaces. The surface clusters used in the current work are shown in Figure 8. Further details on the clusters and ethanol reactions are found in the Supporting Information (Figures S9–S13). In these calculations we ignored the effect of aqueous environment or assumed the ethanol reference state to be gas phase. This simplified approach is often used as a starting point to understanding catalytic reactions in real-world conditions. The initial dehydrogenation of adsorbed ethanol may proceed to produce three different products, CH_3CH_2O, CH_3CHOH, or CH_2CH_2OH as shown in the following pathways:

$$*CH_3CH_2OH \rightarrow *CH_3CH_2O + *H \qquad (1)$$

$$*CH_3CH_2OH \rightarrow *CH_3CHOH + *H \qquad (2)$$

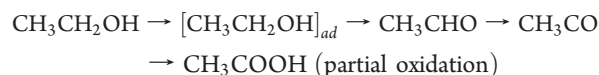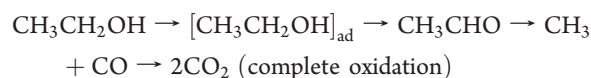$$*CH_3CH_2OH \rightarrow *CH_2CH_2OH + *H \qquad (3)$$

We calculated reaction energies for these processes and report them in Figure 8. For these simplified calculations we have not

calculated activation energies but expect the activation energies to be proportional to the reaction energies, in accord with Brønsted–Evans–Polanyi relation (see for example refs 78 and 79). That is, lower reaction energies will tend to have lower reaction barriers.

Our preliminary data show that the presence of Sn, either through a pure Sn surface or Sn in an Ir–Sn alloy, destabilizes the reaction intermediates to the point of the intermediates being unstable on the surface. On the other hand, both Ir and SnO_2 display reaction energies that are reasonably exothermic, with the dehydrogenation reaction over SnO_2 being very exothermic. It should be emphasized that the DFT calculations shown here are preliminary and certainly do not provide a complete picture of ethanol oxidation, and further work is needed to clarify the reaction mechanism. However, it is reasonable to conclude: (1) Ir-based materials might act as good catalysts for ethanol oxidation; (2) SnO_2 on the surface may further enhance the catalytic performance due to its high tendency to dehydrogenate the ethanol via a α-C–H bond scission step (eq 2); and (3) Sn metal is inactive toward dehydrogenation of ethanol. The DFT calculations support the picture of $Ir/Ir–Sn/SnO_2$ being the active phase of the catalyst.

3.7. Final Product of EOR on Ir-Sn/C. Electrooxidation of ethanol is a complex reaction because several reaction products and intermediates form. Several in situ techniques, such as differential electrochemical mass spectrometry (DEMS) and Fourier transform infrared spectroscopy (FTIRS), have been used to study the reaction mechanism of ethanol electrooxidation by identifying the adsorbed intermediates on the catalysts at the different potentials.[8,9,55,70,80−82] It has been concluded that the oxidation mechanism of ethanol in acidic solution involves two major series of parallel reactions, in which carbon dioxide or acetic acid is the final product:

$$CH_3CH_2OH \rightarrow [CH_3CH_2OH]_{ad} \rightarrow CH_3CHO \rightarrow CH_3$$
$$+ CO \rightarrow 2CO_2 \text{ (complete oxidation)}$$

$$CH_3CH_2OH \rightarrow [CH_3CH_2OH]_{ad} \rightarrow CH_3CHO \rightarrow CH_3CO$$
$$\rightarrow CH_3COOH \text{ (partial oxidation)}$$

Although the nature of ethanol oxidation on the surface of an Ir–Sn alloy catalyst is unclear, it is speculated that its reaction pathway may be similar to that on its Pt–Sn alloy counterpart. To assess the possible reaction mechanism of EOR on Ir–Sn surface, electroactivities of $Ir_{71}Sn_{29}/C$, Pt/C, and Ir/C in the presence of acetaldehyde, acetic acid, and ethanol have been studied, respectively. CV data show: (1) acetaldehyde oxidation on Ir–Sn at low-potential range resembles the polarization curves when the ethanol was used as fuel; (2) only $Ir_{71}Sn_{29}/C$ was active toward the oxidation of acetaldehyde (Figure 9b); and (3) $Ir_{71}Sn_{29}/C$, Ir/C, and Pt/C were all inactive toward acetic acid (Figure 9c). These data strongly indicate that the peaks appearing at ∼0.07 V during the ethanol oxidation reaction on the surface of $Ir_{71}Sn_{29}/C$ can be attributed mainly to the oxidation of ethanol into acetic acid in the presence of Sn and that the final product could be acetic acid via a partial oxidation, in good agreement with the Tafel measurements shown in Figure 5c. Similar results were also reported for a Pt–Sn alloy counterpart catalyst reported from Lamy and co-workers.[83] They found that the formation of CO_2 and acetaldehyde decreased on a Pt–Sn alloy surface compared to pure Pt at low temperature, whereas the formation of acetic acid increased. They explained
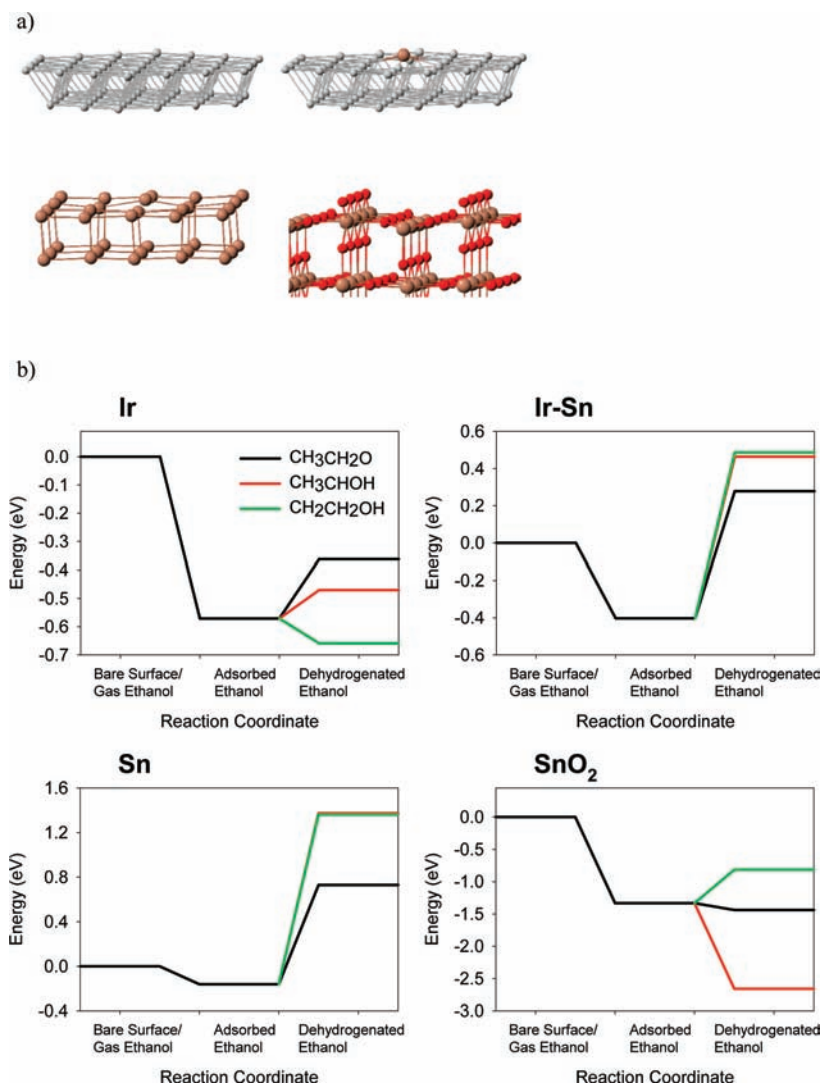
Figure 8. (a) Surface cluster models used in the current work for modeling ethanol dehydrogenation. Gray spheres represent Ir atoms, brown spheres represent Sn atoms, and red spheres represent O atoms. Ir(111), Ir−Sn(111), Sn(100), and SnO_2(110) surfaces are shown. (b) Calculated energies for adsorption of ethanol and reaction (H removal). Note that for Sn, CH_2CH_2OH, and CH_3CHOH have nearly identical reaction energies.
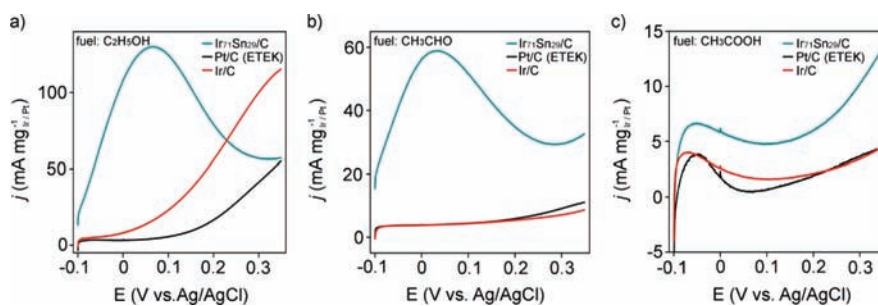
Figure 9. CVs of $Ir_{71}Sn_{29}$/C, Pt/C (ETEK) and Ir/C in 0.5 M of: (a) ethanol, (b) acetaldehyde (c) acetic acid in the presence of 0.5 M of H_2SO_4.

that once acetaldehyde formed on the Pt sites, C−C cleavage was not favored in the presence of alloyed Sn. Acetaldehyde was quickly oxidized into acetic acid in the presence of OH species before the breaking of the C−C to form CH_3 and CO, since adjacent Sn can activate water molecules at very low potential.[83]

Previous in situ differential electrochemical mass spectrometry (DEMS) studies showed that the selectivity for complete oxidation to CO_2 is only about 1% at the potentials up to 1.1 V [vs reversible hydrogen electrode (RHE)] on the surface of Pt_3Sn/C alloy at room temperature in an acid medium, with the major products being acetaldehyde and acetic acid.[69] Since formations

15181

dx.doi.org/10.1021/ja205649z |*J. Am. Chem. Soc.* 2011, 133, 15172–15183

of acetaldehyde and acetic acid deliver only 2 and 4 electrons, compared to the 12 electrons upon the formation of CO_2, the efficiency of incomplete EOR is low. Therefore, studying and developing anode catalysts for highly efficient oxidation of ethanol into CO_2 are a challenge that requires detailed, fundamental understanding of the EOR reaction mechanisms.

While our data show that a higher alloying level between Ir and Sn results in larger ethanol oxidation currents, detailed in situ analysis of the distribution of products (acetic acid, acetaldehyde, CO_2) at given potential is necessary in the future to further understand the role of SnO_2 and Ir—Sn alloy in the oxidation of ethanol oxidation, in order to elucidate the effects of Ir—Sn heterogeneous structures on the reaction mechanism.

4. CONCLUSION

In this paper, we demonstrated the "surfactant-free" synthesis of carbon-supported Ir—Sn/C binary alloy nanoparticles via the polyol process. Compared to commercial Pt/C and PtRu/C benchmark catalysts as well as homemade Pt—Sn/C, superior electroactivity and stability were found in Ir—Sn/C from the CV and current density vs time measurements. Our results, obtained from several characterization techniques, including DFT calculations and electrochemical measurements, allow us to uncover the correlation between the Ir—Sn/C heterogeneous structure and electroactivity in EOR. Our findings include the following: (1) The $Ir_{71}Sn_{29}$/C catalyst consists of an Ir core-rich, Ir—Sn alloy shell-rich, and SnO_2 present on the surface, indicating an Ir/Ir—Sn/SnO_2 heterogeneous structure. In particular, the maximum metallic Sn content alloying with Ir is found to be around 20%. (2) The $Ir_{71}Sn_{29}$/C catalyst showed a very low peak potential (0.07 V vs Ag/AgCl) during EOR, which is mainly due to the formation of acetic acid without breaking of the C—C bond. (3) Both the Ir—Sn alloy and SnO_2 on the surface are important in the EOR, demonstrated by our electrochemical measurements and DFT calculations. In particular, higher level of Ir—Sn alloying resulted in higher mass density in both CV and current density vs time measurements.

Our results will have a significant impact on DEFCs technology by completely replacing Pt with an alternative low-cost, highly active Ir-based nanocatalyst. Our results not only highlight the intriguing structure—function correlation in catalyst design for DEFCs but also for the fundamental catalysis that drives so many processes. The reported findings will directly support the nation's effort to diversify its energy supply portfolio and will help to reduce the global carbon footprint, by offering a more cost-effective DEFC technology.

ASSOCIATED CONTENT

S **Supporting Information.** Synthesis of Ir/Sn and Pt/Sn nanoparticles with varied stoichiometries, EDS (Figure S1), HAADF images and EELS line scans of $Ir_{71}Sn_{29}$ nanoparticles (Figure S2), XPS (Figure S3), in situ XANES spectra (Figure S4), EXAFS spectra (Figure S5), XRD pattern of $Ir_{71}Sn_{29}$/C after thermal treatment in air (Figure S6), CV curves of all Ir—Sn/C catalysts (Figure S7), and TEM images of $Ir_{46}Sn_{54}$/C, $Ir_{55}Sn_{45}$/C, $Ir_{82}Sn_{18}$/C, Ir/C, $Pt_{77}Sn_{23}$/C (Figure S8), and details of ethanol oxidation on the clusters of Ir, Ir—Sn, Sn, SnO_2 (Figure S9—S13). This material is available free of charge via the Internet at http://pubs.acs.org.

AUTHOR INFORMATION

Corresponding Author
xw.teng@unh.edu

REFERENCES

(1) Parsons, R.; Vandernoot, T. *J. Electroanal. Chem.* **1988**, *257* (1—2), 9—45.

(2) Antolini, E. *Mater. Chem. Phys.* **2003**, *78* (3), 563—573.

(3) Lamy, C.; Belgsir, E. M.; Leger, J. M. *J. Appl. Electrochem.* **2001**, *31* (7), 799—809.

(4) Zhou, W. J.; Zhou, Z. H.; Song, S. Q.; Li, W. Z.; Sun, G. Q.; Tsiakaras, P.; Xin, Q. *Appl. Catal., B* **2003**, *46* (2), 273—285.

(5) Vigier, F.; Coutanceau, C.; Perrard, A.; Belgsir, E. M.; Lamy, C. *J. Appl. Electrochem.* **2004**, *34* (4), 439—446.

(6) Antolini, E. *J. Power Sources* **2007**, *170* (1), 1—12.

(7) Kowal, A.; Gojkovic, S. L.; Lee, K. S.; Olszewski, P.; Sung, Y. E. *Electrochem. Commun.* **2009**, *11* (4), 724—727.

(8) Kowal, A.; Li, M.; Shao, M.; Sasaki, K.; Vukmirovic, M. B.; Zhang, J.; Marinkovic, N. S.; Liu, P.; Frenkel, A. I.; Adzic, R. R. *Nat. Mater.* **2009**, *8* (4), 325—330.

(9) Li, M.; Kowal, A.; Sasaki, K.; Marinkovic, N.; Su, D.; Korach, E.; Liu, P.; Adzic, R. R. *Electrochim. Acta* **2010**, *55* (14), 4331—4338.

(10) Bittinscattaneo, B.; Wilhelm, S.; Cattaneo, E.; Buschmann, H. W.; Vielstich, W. *Ber. Bunsen-Ges.* **1988**, *92* (11), 1210—1218.

(11) Hable, C. T.; Wrighton, M. S. *Langmuir* **1993**, *9* (11), 3284—3290.

(12) Xia, X. H.; Liess, H. D.; Iwasita, T. *J. Electroanal. Chem.* **1997**, *437* (1—2), 233—240.

(13) Casado-Rivera, E.; Volpe, D. J.; Alden, L.; Lind, C.; Downie, C.; Vazquez-Alvarez, T.; Angelo, A. C. D.; DiSalvo, F. J.; Abruna, H. D. *J. Am. Chem. Soc.* **2004**, *126* (12), 4043—4049.

(14) Maksimuk, S.; Yang, S. C.; Peng, Z. M.; Yang, H. *J. Am. Chem. Soc.* **2007**, *129* (28), 8684—8685.

(15) Nilekar, A. U.; Xu, Y.; Zhang, J. L.; Vukmirovic, M. B.; Sasaki, K.; Adzic, R. R.; Mavrikakis, M. *Top. Catal.* **2007**, *46* (3—4), 276—284.

(16) Lim, B.; Jiang, M.; Camargo, P. H. C.; Cho, E. C.; Tao, J.; Lu, X.; Zhu, Y.; Xia, Y. *Science* **2009**, *324*, 1302—1305.

(17) Peng, Z. M.; Yang, H. *J. Am. Chem. Soc.* **2009**, *131* (22), 7542.

(18) Strasser, P.; Koh, S.; Anniyev, T.; Greeley, J.; More, K.; Yu, C. F.; Liu, Z. C.; Kaya, S.; Nordlund, D.; Ogasawara, H.; Toney, M. F.; Nilsson, A. *Nat. Chem.* **2010**, *2* (6), 454—460.

(19) Du, W. X.; Wang, Q.; Su, D.; Frenkel, A. I.; Teng, X. W. *Cryst. Growth Des.* **2011**, *11* (2), 594—599.

(20) Brown, L. F. *Int. J. Hydrog. Energy* **2001**, *26* (4), 381—397.

(21) Dohle, H.; Schmitz, H.; Bewer, T.; Mergel, J.; Stolten, D. *J. Power Sources* **2002**, *106* (1—2), 313—322.

(22) Bianchini, C.; Shen, P. K. *Chem. Rev.* **2009**, *109* (9), 4183—4206.

(23) Coutanceau, C.; Demarconnay, L.; Lamy, C.; Leger, J. M. *J. Power Sources* **2006**, *156* (1), 14—19.

(24) Shao, M. H.; Sasaki, K.; Adzic, R. R. *J. Am. Chem. Soc.* **2006**, *128* (11), 3526–3527.

(25) Simoes, M.; Baranton, S.; Coutanceau, C. *Appl. Catal., B* **2011**, *93* (3−4), 354–362.

(26) Colmati, F.; Antolini, E.; Gonzalez, E. R. *J. Solid State Electrochem.* **2008**, *12* (5), 591–599.

(27) Greeley, J.; Mavrikakis, M. *Nat. Mater.* **2004**, *3* (11), 810–815.

(28) Greeley, J.; Mavrikakis, M. *Catal. Today* **2006**, *111* (1−2), 52–58.

(29) Luo, J.; Maye, M. M.; Lou, Y. B.; Han, L.; Hepel, M.; Zhong, C. J. *Catal. Today* **2002**, *77* (1−2), 127–138.

(30) Zhong, C. J.; Maye, M. M. *Adv. Mater.* **2001**, *13* (19), 1507–1511.

(31) Hammer, B.; Hansen, L. B.; Norskov, J. K. *Phys. Rev. B* **1999**, *59* (11), 7413–7421.

(32) Mansour, A. N.; Cook, J. W.; Sayers, D. E. *J. Phys. Chem.* **1984**, *88* (11), 2330–2334.

(33) Fatih, K.; Neburchilov, V.; Alzate, V.; Neagu, R.; Wang, H. *J. Power Sources* **2010**, *195* (21), 7168–7175.

(34) Ohyama, K.; Sugino, T.; Nitta, T.; Kimura, C.; Aoki, H. *Electrochim. Acta* **2011**, *174* (4), 45–50.

(35) *Platinum Today*; Johnson Matthey: London; http://www.platinum.matthey.com/. (accessed June 13, 2011).

(36) Cao, L.; Sun, G. Q.; Li, H. Q.; Xin, Q. *Electrochem. Commun.* **2007**, *9* (10), 2541–2546.

(37) Takasu, Y.; Yoshinaga, N.; Sugimoto, W. *Electrochem. Commun.* **2008**, *10* (4), 668–672.

(38) Qiao, J. L.; Lin, R.; Li, B.; Ma, J. X.; Liu, J. S. *Electrochim. Acta* **2010**, *55* (28), 8490–8497.

(39) Zheng, J. S.; Wang, X. Z.; Qiao, J. L.; Yang, D. J.; Li, B.; Li, P.; Iv, H.; Ma, J. X. *Electrochem. Commun.* **2010**, *12* (1), 27–31.

(40) Bock, C.; Paquet, C.; Couillard, M.; Botton, G. A.; MacDougall, B. R. *J. Am. Chem. Soc.* **2004**, *126* (25), 8028–8037.

(41) Newville, M. *Journal of Synchrotron Radiation* **2001**, *8*, 322–324.

(42) *CP2K*; berliOS: Berlin, Germany; http://cp2k.berlios.de. (accessed June 13, 2011).

(43) VandeVondele, J.; Krack, M.; Mohamed, F.; Parrinello, M.; Chassaing, T.; Hutter, J. *Comput. Phys. Commun.* **2005**, *167* (2), 103–128.

(44) Lippert, G.; Hutter, J.; Parrinello, M. *Mol. Phys.* **1997**, *92* (3), 477–487.

(45) Goedecker, S.; Teter, M.; Hutter, J. *Phys. Rev. B* **1996**, *54* (3), 1703–1710.

(46) Krack, M. *Theor. Chem. Acc.* **2005**, *114* (1−3), 145–152.

(47) VandeVondele, J.; Hutter, J. *J. Chem. Phys.* **2007**, *127*, (11).

(48) Perdew, J. P.; Burke, K.; Ernzerhof, M. *Phys. Rev. Lett.* **1996**, *77* (18), 3865–3868.

(49) Santarossa, G.; Vargas, A.; Iannuzzi, M.; Pignedoli, C. A.; Passerone, D.; Baiker, A. *J. Chem. Phys.* **2008**, *129*, (23).

(50) Psofogiannakis, G.; St-Amant, A.; Ternan, M. *J. Phys. Chem. B* **2006**, *110* (48), 24593–24605.

(51) Santarossa, G.; Iannuzzi, M.; Vargas, A.; Baiker, A. *ChemPhysChem* **2008**, *9* (3), 401–413.

(52) Lamy, C.; Rousseau, S.; Belgsir, E. M.; Coutanceau, C.; Leger, J. M. *Electrochim. Acta* **2004**, *49* (22−23), 3901–3908.

(53) Zhou, W. J.; Song, S. Q.; Li, W. Z.; Zhou, Z. H.; Sun, G. Q.; Xin, Q.; Douvartzides, S.; Tsiakaras, P. *J. Power Sources* **2005**, *140* (1), 50–58.

(54) Antolini, E.; Colmati, F.; Gonzalez, E. R. *J. Power Sources* **2009**, *193* (2), 555–561.

(55) Antolini, E.; Gonzalez, E. R. *Catal. Today* **2011**, *160* (1), 28–38.

(56) Grandjean, D.; Benfield, R. E.; Nayral, C.; Erades, L.; Soulantica, K.; Maisonnat, A.; Chaudret, B. *Phys. Scr.* **2005**, *T115*, 699–702.

(57) Borgna, A.; Stagg, S. M.; Resasco, D. E. *J. Phys. Chem. B* **1998**, *102* (26), 5077–5081.

(58) Kim, J. H.; Choi, S. M.; Nam, S. H.; Seo, M. H.; Choi, S. H.; Kim, W. B. *Appl. Catal., B* **2008**, *82* (1−2), 89–102.

(59) Ramallo-Lopez, J. M.; Santori, G. F.; Giovanetti, L.; Casella, M. L.; Ferretti, O. A.; Requejo, F. G. *J. Phys. Chem. B* **2003**, *107* (41), 11441–11451.

(60) Frenkel, A. *Z. Kristallogr.* **2007**, *222* (11), 605–611.

(61) Du, W. X.; Wang, Q.; LaScala, C.; Zhang, L. H.; Su, D.; Frenkel, A. I.; Teng, X. W. *J. Mater. Chem.* **2011**, *21*, 8887–8892.

(62) Fernandez-Garcia, M.; Martinez-Arias, A.; Hanson, J. C.; Rodriguez, J. A. *Chem. Rev.* **2004**, *104* (9), 4063–4104.

(63) Jiang, L.; Hsu, A.; Chu, D.; Chen, R. *Int. J. Hydrogen Energy* **2011**, *35* (1), 365–372.

(64) Babu, P. K.; Kim, H. S.; Oldfield, E.; Wieckowski, A. *J. Phys. Chem. B* **2003**, *107* (31), 7595–7600.

(65) Bergamaski, K.; Gonzalez, E. R.; Nart, F. C. *Electrochim. Acta* **2008**, *53* (13), 4396–4406.

(66) Vigier, F.; Coutanceau, C.; Hahn, F.; Belgsir, E. M.; Lamy, C. *J. Electroanal. Chem.* **2004**, *563* (1), 81–89.

(67) Jiang, L. H.; Sun, G. Q.; Sun, S. G.; Liu, J. G.; Tang, S. H.; Li, H. Q.; Zhou, B.; Xin, Q. *Electrochim. Acta* **2005**, *50* (27), 5384–5389.

(68) Colmati, F.; Antolini, E.; Gonzalez, E. R. *J. Power Sources* **2006**, *157* (1), 98–103.

(69) Wang, H.; Jusys, Z.; Behm, R. J. *J. Power Sources* **2006**, *154* (2), 351–359.

(70) Jiang, L.; Colmenares, L.; Jusys, Z.; Sun, G. Q.; Behm, R. J. *Electrochim. Acta* **2007**, *53* (2), 377–389.

(71) Antolini, E.; Gonzalez, E. R. *Electrochim. Acta* **2010**, *55* (22), 6485–6490.

(72) Colmenares, L.; Wang, H.; Jusys, Z.; Jiang, L.; Yan, S.; Sun, G. Q.; Behm, R. J. *Electrochim. Acta* **2006**, *52* (1), 221–233.

(73) Doye, J. P. K.; Wales, D. J. *New J. Chem.* **1998**, *22* (7), 733–744.

(74) Dinh, H. N.; Ren, X. M.; Garzon, F. H.; Zelenay, P.; Gottesfeld, S. *J. Electroanal. Chem.* **2000**, *491* (1−2), 222–233.

(75) Garcia-Rodriguez, S.; Somodi, F.; Borbath, I.; Margitfalvi, J. L.; Pena, M. A.; Fierro, J. L. G.; Rojas, S. *Appl. Catal., B* **2009**, *91* (1−2), 83–91.

(76) Koper, M. T. M. *Surf. Sci.* **2004**, *548* (1−3), 1–3.

(77) Zhou, W. J.; Li, W. Z.; Song, S. Q.; Zhou, Z. H.; Jiang, L. H.; Sun, G. Q.; Xin, Q.; Poulianitis, K.; Kontou, S.; Tsiakaras, P. *J. Power Sources* **2004**, *131* (1−2), 217–223.

(78) Bligaard, T.; Norskov, J. K.; Dahl, S.; Matthiesen, J.; Christensen, C. H.; Sehested, J. *J. Catal.* **2004**, *224* (1), 206–217.

(79) Cheng, J.; Hu, P.; Ellis, P.; French, S.; Kelly, G.; Lok, C. M. *J. Phys. Chem. C* **2008**, *112* (25), 9464–9473.

(80) Hitmi, H.; Belgsir, E. M.; Leger, J. M.; Lamy, C.; Lezna, R. O. *Electrochim. Acta* **1994**, *39* (3), 407–415.

(81) Iwasita, T.; Pastor, E. *Electrochim. Acta* **1994**, *39* (4), 531–537.

(82) de Souza, J. P. I.; Queiroz, S. L.; Bergamaski, K.; Gonzalez, E. R.; Nart, F. C. *J. Phys. Chem. B* **2002**, *106* (38), 9825–9830.

(83) Rousseau, S.; Coutanceau, C.; Lamy, C.; Leger, J. M. *J. Power Sources* **2006**, *158* (1), 18–24.